*Dental Materials Journal 2024; 43(6): 755–761*

# Corrosion behavior of Zr-14Nb-5Ta-1Mo alloy in simulated body fluid

Tomoyo MANAKA[1], Yusuke TSUTSUMI[2], Maki ASHIDA[3], Peng CHEN[4] and Takao HANAWA[5,6,7]

[1] *Aluminium Research Center, University of Toyama, 3190 Gofuku, Toyama, Toyama 930-8555, Japan*
[2] *Research Center for Structural Materials, National Institute for Materials Science, 1-2-1 Sengen, Tsukuba, Ibaraki 305-0047, Japan*
[3] *Faculty of Science and Technology, Seikei University, 3-3-1 Kichijoji-Kitamachi, Musashino, Tokyo 180-8633, Japan*
[4] *Graduate School of Dentistry, Tohoku University, 4-1 Seiryo-machi, Aoba-ku, Sendai, Miyagi 980-8575, Japan*
[5] *Tokyo Medical and Dental University, 1-5-45 Yushima, Chiyoda, Tokyo 113-8510, Japan*
[6] *Division of Materials and Manufacturing Science, Graduate School of Engineering, Osaka University, 2-1 Yamadaoka, Suita, Osaka 565-0871, Japan*
[7] *Department of Medical Device Engineering, Graduate School of Medicine, Kobe University, 7-5-1 Kusunoki-cho, Kobe, Hyogo 650-0017, Japan*
*Corresponding author, Tomoyo MANAKA; E-mail: manaka@sus.u-toyama.ac.jp*

Metals that are used to reconstruct skeletal structures often interfere with magnetic resonance imaging (MRI) owing to differences in magnetic susceptibility; consequently, metals with lower magnetic susceptibilities need to be developed for use in implant devices. Herein, we investigated the corrosion properties of the Zr-14Nb-5Ta-1Mo alloy, which exhibits low magnetic susceptibility and excellent mechanical properties. The pitting potential of Zr-14Nb-5Ta-1Mo was higher than that of pure Zr. The passive current density of Zr-14Nb-5Ta-1Mo also higher than that of pure Zr, which is ascribable to slow reconstruction of the initial passive film associated with the presence of Nb and Ta. XPS revealed that the passive film is enriched with Nb and Ta. Therefore, while the Zr-14Nb-5Ta-1Mo alloy exhibited a high initial passive current density in simulated body fluid, it formed a stable passive film that suppressed localized corrosion. Zr-14Nb-5Ta-1Mo is therefore a prospective implant-material alloy candidate.

*Keywords*: Zirconium alloy, Corrosion resistance, Passive film

## INTRODUCTION

Metals are often used to reconstruct skeletal structures that require load-bearing capacities[1,2] because they exhibit balanced strengths and ductilities. However, while magnetic resonance imaging (MRI) is widely used for surgical diagnoses, MR images captured near metallic implants show defects ascribable to artifacts resulting from differences in the magnetic susceptibilities of biological tissue and metals[3-6]. Furthermore, artifact volume is directly proportional to the magnetic susceptibility difference between those of metallic implant and biological tissue around. Consequently, the magnetic susceptibilities of the metals used in implant devices need to be reduced. In addition, metallic biomaterials require low Young's modulus to prevent bone resorption.

Zr alloys have recently been investigated for use in medical devices. Zr resides in the fourth group of the periodic table along with Ti, which is widely used in dental and medical devices. Therefore, Zr and Ti have similar mechanical and chemical properties. Furthermore, Zr is poorly cytotoxic compared to other conventional metals; consequently, Zr alloys are considered to be biosafe metallic materials. The magnetic susceptibility of Zr is also lower than those of other metallic biomaterials; indeed, the magnetic susceptibility of pure Zr has been reported to be approximately thirty-times lower than that of type 316L stainless steel, seven-times lower than that of a Co-Cr-Mo alloy, and approximately half that of Ti[7-10]. In addition, the properties of Zr are superior to those of Ti for medical applications. *In vivo*, Zr combines with phosphate ions to form zirconium phosphate, which is stable and protective; consequently, calcium ions are not incorporated and calcium phosphate is less likely to form on the Zr surface[11]. Hence, unlike Ti, Zr is less likely to fuse with bone in the post-implantation period; in other words, devices fabricated using Zr can be removed even after long-term implantation.

Recently, Zr-14Nb-5Ta-1Mo (wt%) was prepared as a new beta-type Zr alloy[12,13]; this alloy was designed using the d-electron alloy design method and exhibited values of $17.34\times10^{-9}$ $m^3kg^{-1}$, 796 MPa, and 61 GPa for magnetic susceptibility, yield stress, and Young's modulus, respectively. Indeed, this alloy exhibited a lower Young's modulus and a lower magnetic susceptibility than the Ti-6Al-4V alloy. In addition, the Zr-14Nb-5Ta-1Mo alloy exhibits good cytocompatibility and osteoconductivity[14]. However, the corrosion resistance of this alloy needs to be evaluated for dental and medical applications, as metallic-biomaterial corrosion can induce fatigue, wear, and fretting in an implanted device, which may seriously harm the patient (*e.g.*, metal allergy). Zr forms a passive film on its surface; therefore, Zr is highly corrosion resistant in both acidic and alkaline solutions. However, pitting corrosion occurs on Zr surface in the chloride ions containing environments, initiated by inclusions[15-18]. Zr-alloy devices are in constant contact with chloride ions *in vivo* because $Cl^-$ is present in all living body. Therefore, the corrosion resistance of the Zr-14Nb-5Ta-1Mo alloys needs to be evaluated to ensure biological safety. In this study, we investigated the corrosion resistance of the Zr-14Nb-5Ta-1Mo alloy in simulated body fluid and analyzed its passive film.

Received May 30, 2024: Accepted Jul 2, 2024
doi:10.4012/dmj.2024-158 JOI JST.JSTAGE/dmj/2024-158

This is an open access article under the CC BY license
https://creativecommons.org/licenses/by/4.0/

## MATERIALS AND METHODS

*Specimen preparation*

The chemical compositions of the prepared Zr-14Nb-5Ta-1Mo (wt%) alloy and pure Zr plate are listed in Table 1. The theoretical design of the Zr-14Nb-5Ta-1Mo alloy was described in a previous report[12]. The alloy was dissolved using the cold crucible-induced melting (CCIM) technique using pure Zr crystal bars (99.94%), Zr sheets (97.38%), Nb chips (99.87%), Ta chips (99.98%), and Mo wire (99.95%). Each ingot was dissolved for 20 min and furnace-cooled for 1 h in an Ar atmosphere, after which it was inverted, remelted, and cooled in an Ar atmosphere. The ingot was then inverted, melted for 20 min, and cooled under vacuum. The ingot had a diameter 130 mm and weighed 6 kg. The melted ingot was hot-forged using a forge-heating furnace and a 1-t air hammer. After being heated in a furnace at 1,323 K for 1 h, the ingot was drawn to a diameter of 32 mm. Lathing was then performed to obtain a hot-forged material with a diameter of 24 mm. As a comparison material, Zr-14Nb-5Ta alloy specimen and pure Zr plate (99.5%) were also prepared. Zr-14Nb-5Ta alloy specimen was melted and processed in the same method as the Zr-14Nb-5Ta-1Mo alloy.

The ingots and plates were cut to a thickness of 1 mm and used as specimens. The surfaces of the corrosion-evaluation specimens were mechanically ground using #150-, #320-, #600-, and #800-grit abrasive SiC papers. The surface of each passive-film-analysis specimen was polished to a mirror finish by mechanical grinding with #800-grit abrasive SiC paper, followed by buffing with a colloidal silica suspension. The specimens were then ultrasonicated twice in acetone and once in isopropanol for 600 s (each). The specimens were immersed in ultrapure water for 24 h at room temperature to stabilize the passive film[15].

*Corrosion resistance evaluation*

Corrosion resistance was evaluated using anodic polarization measurement which were conducted according to the JIS T0302 Japanese standard testing method. In addition to the Zr alloy, the corrosion resistances of pure Mo, pure Nb, and pure Ta, of which the Zr-14Nb-5Ta-1Mo alloy is composed of, were also evaluated. For comparison, the corrosion resistance of commercially pure (CP) Ti (grade 2), prepared using the same method used to polish the Zr alloy, was also evaluated. A specimen holder composed of polytetrafluoroethylene (PTFE) and acrylic resin[19] was used as the working electrode, with the specimen and O-ring fixed to the holder. The measured area was 0.353 $cm^2$. Pt plate and Ag/AgCl (in saturated aqueous KCl) were used as counter and reference electrodes, respectively. Measurements were performed using an electrochemical measurement system (HZ-7000, Meiden Hokuto, Tokyo, Japan) with a saline (0.9% aqueous NaCl) measurement solution used as the simulated body fluid. The solution temperature was maintained at 310 K. The final open-circuit potential, which was measured after 600 s of immersion in the solution, was taken as the corrosion potential ($E_{corr}$). A potential was applied at −100 mV relative to $E_{corr}$, and a linearly increasing anodic potential scan was initiated at 1 mV $s^{-1}$. A rapid increase in current due to pitting corrosion was recorded. The experiment was terminated when the current density reached 10 mA $cm^{-2}$. These experiments were repeated five times for each alloy to evaluate reproducibility. The pitting potential ($E_{pit}$) was determined from the polarization curve, and is defined as the potential at which a current density of 100 μA $cm^{-2}$ was recorded.

*Passive-film analysis*

Passive films were analyzed using X-ray photoelectron spectroscopy (XPS; JPS-9010MC, JEOL, Tokyo, Japan) using untreated and surface-treated pure Zr and Zr-14Nb-5Ta-1Mo-alloy specimens. The surface treatments were polarization for 1 h at a constant potential of 0.4 or 1.0 V in saline to reveal changes in the passive film in solution. All binding energies reported in the present work are relative to the Fermi level ($E_F$), and all spectra were recorded following excitation using a MgKα source (1,253.6 eV), with the accelerator voltage and current set to 10 kV and 10 mA, respectively. Pass energies of 50 and 20 eV were used for the wide and narrow scans, respectively. The measurement chamber was maintained at an ultrahigh vacuum of $3.0\times10^{-7}$ Pa or lower, and a 90° detection angle relative to the specimen surface was used. All binding energies were calibrated against the C 1s peak ascribable to adventitious carbon (285.0 eV). Shirley's method[20] was used to calculate the integrated peak intensities, which involved subtracting the background from the recorded spectrum, and CasaXPS Version 2.3.12 (computer aided surface analysis for X-ray photoelectron spectroscopy) was used to deconvolute the spectra. The chemical composition and thickness of each passive film were determined from the intensities of the integrated peaks in each spectrum[21,22]; target XPS spectra included: C 1s, O 1s, Zr $3d_{5/2}$, Nb $3d_{5/2}$, Ta $4f_{7/2}$, and Mo $3d_{5/2}$.

Table 1 Chemical compositions of pure Zr and the Zr-14Nb-5Ta-1Mo alloy

| Specimen | Composition (wt%) | | | | | | | | | |
|---|---|---|---|---|---|---|---|---|---|---|
| | Zr | Nb | Ta | Mo | Fe | Cr | C | O | N | H |
| Pure Zr | >99.5 | — | — | — | 0.045 | 0.006 | 0.004 | 0.072 | 0.004 | 0.004 |
| Zr-14Nb-5Ta-1Mo alloy | Bal. | 13.5 | 4.98 | 0.97 | <0.01 | <0.01 | <0.01 | 0.044 | 0.010 | 0.010 |

## RESULTS

*Polarization measurements*

Figure 1 (A) shows polarization curves for the Zr-14Nb-5Ta-1Mo alloy, pure Zr, and pure Ti, which reveals pitting corrosion in the Zr-14Nb-5Ta-1Mo alloy and pure Zr specimens, with none observed for pure Ti. Only one polarization curve was shown for pure Ti because no variations were observed. Pure Zr was determined to have an average $E_{pit}$ of 0.83±0.30 V (varying between 0.50 and 1.10 V). The pitting corrosion observed for pure Zr at relatively low potentials reveals that an *in-vivo* pitting risk exists. On the other hand, the average $E_{pit}$ value for the Zr-14Nb-5Ta-1Mo alloy was determined to be 1.85±0.23 V (varying between 1.60 and 2.20 V), which is higher than that of pure Zr.

The polarization curve acquired for the Zr-14Nb-5Ta-1Mo alloy exhibits specific behavior: the initial current density was observed to be higher than that of pure Zr and decreased slightly with increasing applied potential. The current density at 0.4 V, where both the Zr-14Nb-5Ta-1Mo alloy and pure Zr exhibit passivity, is defined as the passive current density ($i_{pass}$). The Zr-14Nb-5Ta-1Mo alloy and pure Zr exhibited average $i_{pass}$ values of 23.3±1.94 and 5.3±0.58 μA cm$^{-2}$, respectively. Pure Nb, pure Ta, and pure Mo, which are constituents of the alloy, were subjected to anodic polarization measurements to determine the reason for the high $i_{pass}$ value associated with the Zr-14Nb-5Ta-1Mo alloy. Figure 2 shows polarization curves for pure Nb, pure Ta, and pure Mo. Only one polarization curve each for pure Nb, pure Ta, and pure Mo is shown because no variation was observed. Pure Nb and pure Ta exhibited passivation behavior up to 3.0 V when the current was increased from near the corrosion potential. In contrast, the polarization curve for pure Mo showed active dissolution behavior near $E_{corr}$.

The corrosion behavior of the Zr-14Nb-5Ta (wt%) alloy was also investigated to clarify how Mo effects the initial increase in the $i_{pass}$ value of the Zr-14Nb-5Ta-1Mo alloy. The Zr-14Nb-5Ta alloy was subjected to anodic polarization measurements under the same conditions. Polarization curves for the Zr-14Nb-5Ta alloy and pure Zr are shown in Fig. 1 (B), which reveals that the polarization curves for the Zr-14Nb-5Ta and Zr-14Nb-5Ta-1Mo alloys show similar behavior, with a high initial $i_{pass}$ that slightly decreases with increasing applied potential. The Zr-14Nb-5Ta alloy exhibited an average $i_{pass}$ value of 31.3±1.14 μA cm$^{-2}$.

*Passive-film analysis*

The current density in the passive region depends significantly on the passive film. The passive film of the Zr-14Nb-5Ta-1Mo, Zr-14Nb-5Ta alloy, and pure Zr were analyzed by XPS. Specimens were either untreated or treated under constant potential polarization conditions for 3,600 s at a passivation potential of 0.4 or 1.0 V in saline. XPS survey spectra of the untreated and 0.4-V-polarized specimens are shown in Fig. 3. In addition to

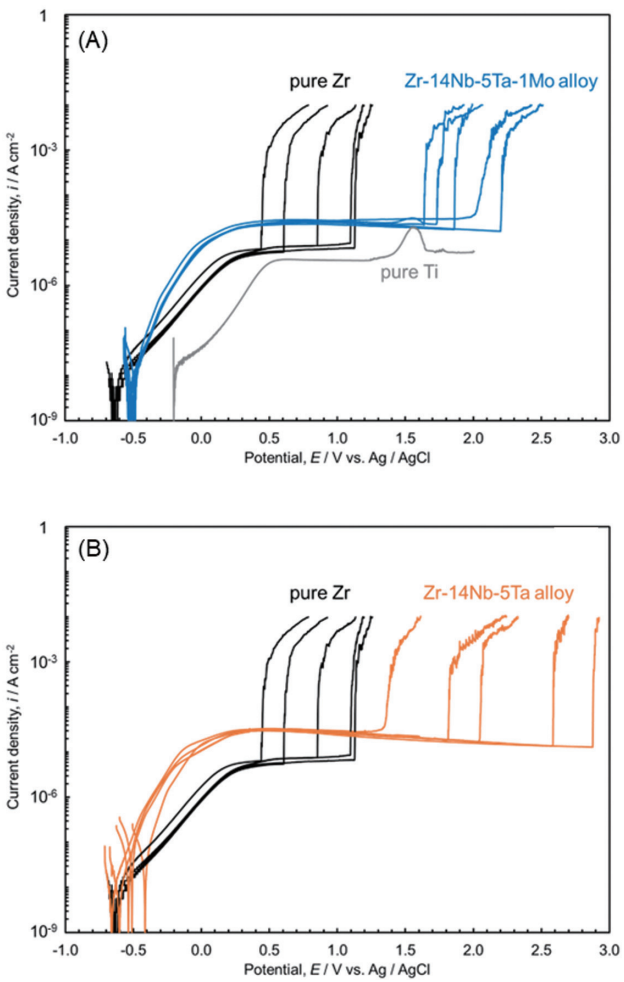


Fig. 1 Polarization curves for the (A) Zr-14Nb-5Ta-1Mo alloy, pure Zr, and pure Ti and (B) Zr-14Nb-5Ta alloy and pure Zr.

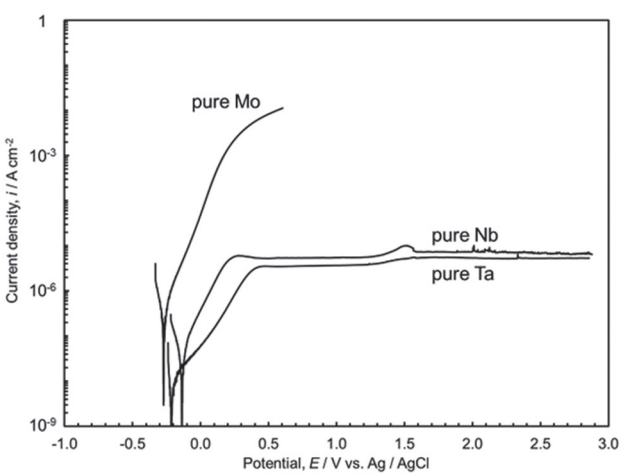


Fig. 2 Polarization curves for pure Nb, pure Ta, and pure Mo, which are alloying elements of the Zr-14Nb-5Ta-1Mo alloy.

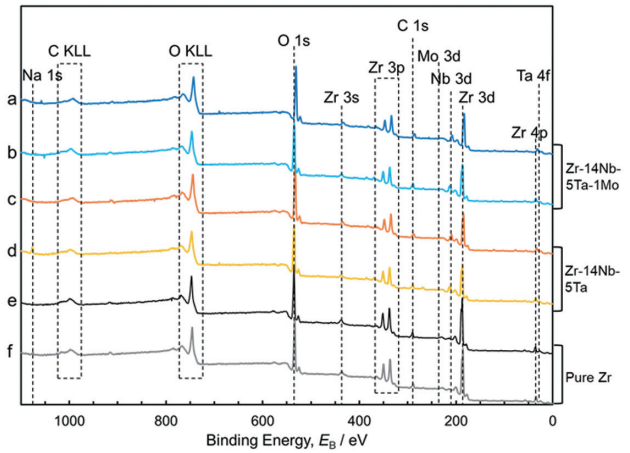


Fig. 3 Wide scan XPS spectra of the: (a) untreated Zr-14Nb-5Ta-1Mo alloy, (b) Zr-14Nb-5Ta-1Mo alloy polarized at 0.4 V, (c) untreated Zr-14Nb-5Ta alloy, (d) Zr-14Nb-5Ta alloy polarized at 0.4 V, (e) untreated pure Zr, and (f) pure Zr polarized at 0.4 V.

peaks derived from the C, O, and Zr in all specimens, peaks associated with Nb, Ta, and Mo were observed in the spectra of the Zr-14Nb-5Ta-1Mo alloy, with a further small peak at approximately 1,072 eV observed for the polarized specimens; this peak corresponds to the Na 1s binding energy[23] and is ascribable to the saline solution used during polarization treatment. Figure 4 shows narrow scan Zr 3d, Nb 3d, Ta 4f, and Mo 3d spectra. The Zr $3d_{5/2}$ peak observed at a binding energy of 182.1 eV reveals that Zr is present in the form of $ZrO_2$[24-29]. No peak corresponding to Zr metal was detected. All specimens exhibited similar peaks in the 178.0–188.0 eV range. The XPS spectra of the Zr-14Nb-5Ta-1Mo and Zr-14Nb-5Ta alloys exhibit peaks derived from Nb at 200.0–214.0 eV; Nb $3d_{5/2}$ peaks separated into $Nb^{2+}$ (201.8 eV), $Nb^{4+}$ (204.7 eV), $Nb^{5+}$ (207.3 eV)[30-33]. No peaks corresponding to metallic Nb were detected on any surface. Peaks derived from Ta were also detected at 17.0–31.0 eV, with O 2s[34] and Zr 4p[35,36] peaks also observed at binding energies close to those observed for Ta 4f. We assumed that the positions, shapes, and areas of the O 2s and

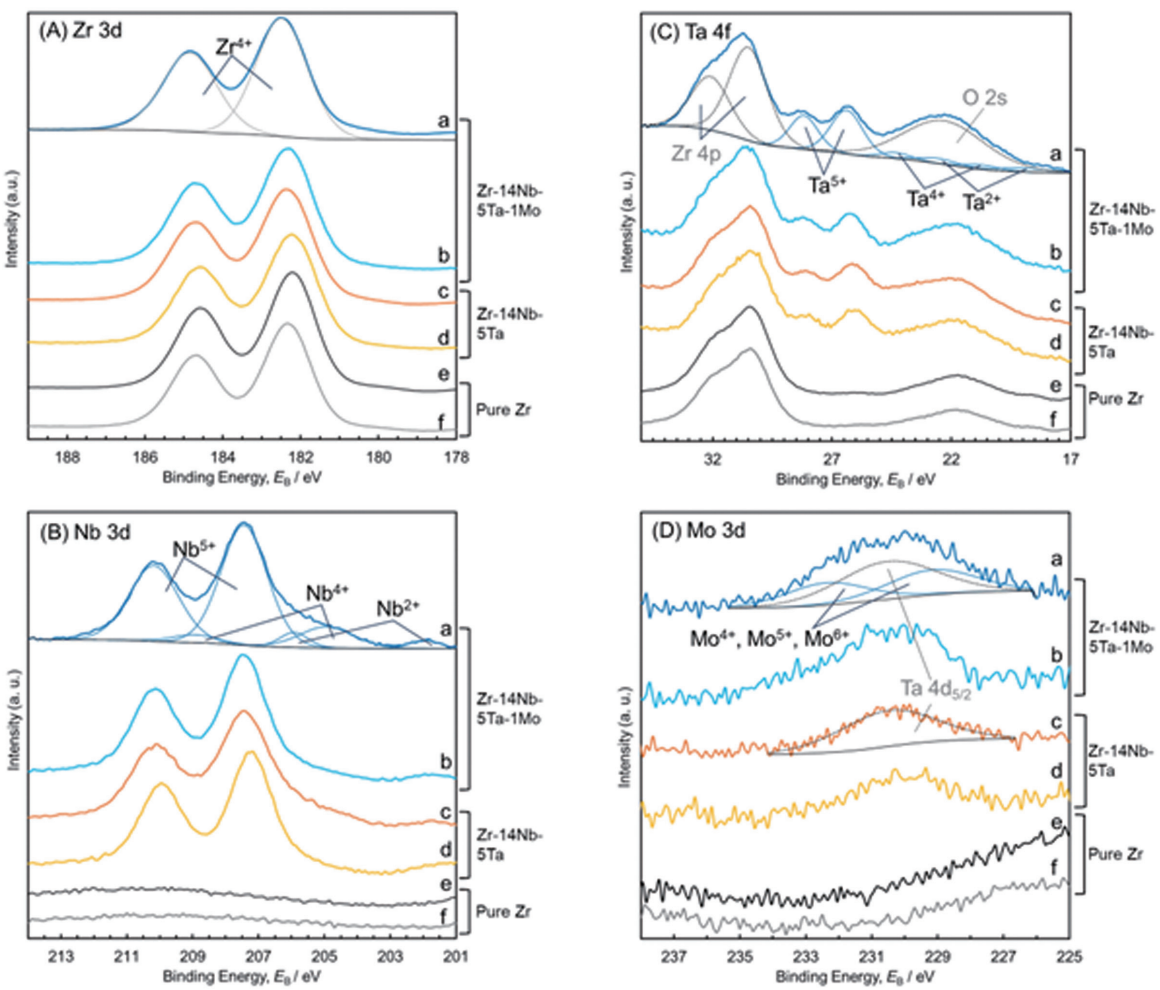


Fig. 4 Narrow scan (A) Zr 3d, (B) Nb 3d, (C) Ta 4f, and (D) Mo 3d XPS spectra of the (a) untreated Zr-14Nb-5Ta-1Mo alloy, (b) Zr-14Nb-5Ta-1Mo alloy polarized at 0.4 V, (c) untreated Zr-14Nb-5Ta alloy, (d) Zr-14Nb-5Ta alloy polarized at 0.4 V, (e) untreated pure Zr, and (f) pure Zr polarized at 0.4 V.

Zr 4p peaks in the spectra of pure Zr and the Zr-14Nb-5Ta-1Mo and Zr-14Nb-5Ta alloys are equivalent. The Ta 4f peaks observed for the Zr-14Nb-5Ta-1Mo and Zr-14Nb-5Ta alloys were analyzed with reference to that of untreated pure Zr. Ta $4f_{7/2}$ binding energies of $Ta^{2+}$ (19.5 eV), $Ta^{4+}$ (21.6 eV), and $Ta^{5+}$ (27.6 eV) were observed[33,37-42]. No peaks corresponding to metallic Ta were detected on any surface. The relative amounts of $Nb^{5+}$ and $Ta^{5+}$ exceeded those of $Nb^{2+}$ and $Nb^{4+}$, and $Ta^{2+}$ and $Ta^{4+}$, respectively, with the same trend observed irrespective of the alloy type or polarization treatment. Peaks corresponding to Mo were detected at 225.0–236.0 eV, with Ta $4d_{5/2}$[43,44] peaks also observed close to the Mo 3d region. We assumed that the Ta $4d_{5/2}$ spectra of the Zr-14Nb-5Ta-1Mo and Zr-14Nb-5Ta alloys are equivalent. The Mo 3d peak observed for the Zr-14Nb-5Ta-1Mo alloy was analyzed with reference to the untreated Zr-14Nb-5Ta alloy, which revealed Mo $3d_{5/2}$ and Mo $3d_{3/2}$ peaks at 229.0 and 232.3 eV, respectively, consistent with the presence of Mo oxides[45-47]. The Mo oxide spectrum contains $Mo^{4+}$, $Mo^{5+}$, and $Mo^{6+}$ peaks; however, the Mo-derived peaks detected in this study were weak, and detailed peak deconvolution was not possible. Therefore, the $Mo^{4+}$, $Mo^{5+}$, and $Mo^{6+}$ peaks were collectively analyzed as "Mo oxides". No peaks corresponding to metallic Mo were detected on any surface.

## DISCUSSION

The pitting corrosion potentials of both pure Zr and Zr-14Nb-5Ta-1Mo alloys varied. The variations in pitting potential are ascribable the exposure of inclusions with different corrosion-inducing properties on the Zr surface[18]. Pitting corrosion on the Zr surface first occur at sites where most corrosion-inducing inclusions are exposed. Inclusions which induce pitting corrosion at low potentials contain Sn, C, and O[17,18], and these inclusions are believed to have been exposed on the pure Zr surface. While the pitting potential of the Zr-14Nb-5Ta-1Mo alloy varied, the lowest pitting potential of this Zr alloy is higher than that of pure Zr. Therefore, the Zr-14Nb-5Ta-1Mo alloy suppressed the formation of pitting-corrosion-inducing inclusions at low potentials; hence, the Zr-14Nb-5Ta-1Mo alloy exhibited superior pitting-corrosion resistance than pure Zr.

The polarization curve acquired for the Zr-14Nb-5Ta-1Mo alloy exhibits a high initial $i_{pass}$ and decreased slightly with increasing applied potential. Anodic polarization measurements of the constituent elements were performed to clarify the high initial $i_{pass}$ values. Pure Nb and pure Ta showed passivation behavior, whereas pure Mo showed active dissolution behavior, as shown in Fig. 2. Thus, it was suggested that the increase in $i_{pass}$ observed at the commencement of the potential sweep is ascribable to the selective dissolution of Mo, with the current density decreasing with decreasing Mo concentration on the surface. The corrosion behavior of the Zr-14Nb-5Ta alloy was also investigated to clarify how Mo effects the initial increase $i_{pass}$ value. The polarization curves for the Zr-14Nb-5Ta exhibited similar behavior to Zr-14Nb-5Ta-1Mo alloys show similar behavior, as shown in Fig. 1 (B). Therefore, the high initial $i_{pass}$ value is not related to the presence or absence of Mo in the alloy.

The effect of passive film on corrosion properties was evaluated. While polarization treatment may have increased the thickness of the passive film, no substrate-metal-derived signals were observed for any of the samples, which indicates that the passive film on each specimen is thicker than the XPS detection depth; consequently, the thickness of each the passive film was unable to be determined in this study. The composition of the passive film was calculated from XPS results. The concentrations of O were found to be similar, irrespective of the Zr alloy type and polarization. Table 2 lists the compositions (at%) of the Zr-14Nb-5Ta-1Mo and Zr-

Table 2 Substrate compositions (at%) and cation fractions in the passive films of pure Zr and the Zr-14Nb-5Ta-1Mo and Zr-14Nb-5Ta alloys

| Substrate composition (at%) | | | | | |
|---|---|---|---|---|---|
| Specimen | | Zr | Nb | Ta | Mo |
| Zr-14Nb-5Ta-1Mo alloy | | 82.3 | 14.1 | 2.6 | 1.0 |
| Zr-14Nb-5Ta alloy | | 83.3 | 14.1 | 2.6 | — |
| pure Zr | | 100 | — | — | — |
| **Cation fraction in the passive film (at%)** | | | | | |
| Specimen | | Zr | Nb | Ta | Mo |
| Zr-14Nb-5Ta-1Mo alloy | Untreated (a) | 80.2±0.6 | 15.2±0.4 | 3.9±0.2 | 0.7±0.1 |
| | Polarized at 0.4 V (b) | 81.0±1.1 | 14.5±0.8 | 3.8±0.2 | 0.7±0.1 |
| Zr-14Nb-5Ta alloy | Untreated (c) | 81.5±0.3 | 14.4±0.5 | 4.1±0.2 | — |
| | Polarized at 0.4 V (d) | 82.8±0.7 | 13.1±1.0 | 4.1±0.3 | — |
| pure Zr | Untreated (e) | 100 | — | — | — |
| | Polarized at 0.4 V (f) | 100 | — | — | — |

14Nb-5Ta alloy substrates and the cation fractions in the passive films on their surfaces. The atomic composition ratios of the substrates were calculated from the weight ratios of the alloys. On the other hand, the cation ratios in the passive films were calculated from the experimental XPS data. The passive-film compositions of the specimens polarized at 1.0 V are equivalent to those of the specimens polarized at 0.4 V. While the passive films have lower Zr and Mo concentration than the substrates, their Nb and Ta concentrations are higher; in other words, the passive films are enriched with Nb and Ta. The Nb and Ta concentrations are also slightly affected by the presence or absence of Mo in each alloy; their concentrations depended on the type of alloy and the polarization-treatment conditions, although no significant differences were observed. As described above, Mo in Zr-14Nb-5Ta-1Mo alloy does not affect corrosion behavior and passive film formation. It is inferred that addition of 1 wt% Mo to Zr-14Nb-5Ta alloy is stabilized the β-phase a little more and can be obtained lower Young's modulus of the alloy, which enabled the Zr-14Nb-5Ta-1Mo alloy to achieve both high strength, low Young's modulus and low magnetic susceptibility[12]. However, the Mo concentration was small as only 1 wt% because Mo has a higher stability of the β-phase compared with other added elements of Nb and Ta. Due to the small Mo content, the presence or absence of Mo had little effect on corrosion properties.

Figure 1 (A) shows that the Zr-14Nb-5Ta-1Mo alloy has a higher $i_{pass}$ value than pure Zr or CP Ti. The passive film is reconstructed following immersion in the test solution, and the higher $i_{pass}$ value for the alloy is believed to be due to the fact that it takes longer to reconstruct and stabilize the passive film on the alloy following immersion than on pure Zr. However, Nb and Ta form stable passive films, as shown in Fig. 2. Furthermore, the addition of Nb and Ta to a Ti alloy has been reported to enrich the passive film with Nb and Ta, resulting in good corrosion resistance. When Ti-Nb-Ta alloys are immersed in a simulated body fluid, the concentration of Nb and Ta in the passive film increases with time due to passive film reconstruction, and the corrosion rate decreases with time[48]. The passive film on the Zr-14Nb-5Ta-1Mo alloy showed similarly enriched Nb and Ta. Therefore, the addition of Nb and Ta to a Zr alloy is believed to improve corrosion resistance, as has been observed for Ti alloys. In addition, although the cytocompatibility of the Zr-14Nb-5Ta-1Mo alloy has been evaluated in its initial passive-film state, it exhibited properties comparable to those of CP Ti[14]. Therefore, the passive film on the Zr-14Nb-5Ta-1Mo alloy exhibited sufficient corrosion resistance, even in its initial state, with corrosion resistance expected to improve over the longer term.

## CONCLUSION

In this study, we evaluated the corrosion properties of the Zr-14Nb-5Ta-1Mo alloy, which exhibits low magnetic susceptibility and a low Young's modulus, in a simulated *in-vivo* environment. Anodic polarization measurements in simulated body fluids and XPS analysis of passive films were performed. The Zr-14Nb-5Ta-1Mo alloy exhibited a higher $E_{pit}$ value than pure Zr, which indicates that it is less likely to undergo pitting corrosion in an *in-vivo* environment because corrosion-inducing-inclusion formation is suppressed. The Zr-14Nb-5Ta-1Mo alloy exhibited a higher initial current density than pure Zr, which decreased slightly with increasing applied potential, and is ascribable to the slow rate associated with the reconstruction of the passive film in the simulated body fluid owing to the presence of Nb and Ta, irrespective of the inclusion or non-inclusion of Mo in the alloy. The Zr-14Nb-5Ta-1Mo-alloy passive film was found to be enriched with Nb and Ta; hence, this alloy forms a stable passive film and exhibits good corrosion resistance in simulated body fluid. The Zr-14Nb-5Ta-1Mo alloy is therefore a prospective implant-material candidate.

## ACKNOWLEDGMENTS

This study was supported by the JSPS KAKENHI (grant numbers 15H03018 and 19H04464). This study was also supported by an Institute of Light Metals (ILM) Joint Usage/Research Grant.

## CONFLICT OF INTEREST

The authors declare no competing interests.

## REFERENCES

1) Hanawa T. Titanium-tissue interface reaction and its control with surface treatment. Front Bioeng Biotechnol 2019; 7: 170.
2) Kaur M, Singh K. Review on titanium and titanium based alloys as biomaterials for orthopaedic applications. Mater Sci Eng C 2019; 102: 844-862.
3) Imai H, Tanaka Y, Nomura N, Tsutsumi Y, Doi H, Kanno Z, *et al*. Three-dimensional quantification of susceptibility artifacts from various metals in magnetic resonance images. Acta Biomater 2013; 9: 8433-8439.
4) Elison JM, Leggitt VL, Thomson M, Oyoyo U, Wycliffee ND. Influence of common orthodontic appliances on the diagnostic quality of cranial magnetic resonance images. Am J Orthod Dentofacial Orthop 2008; 134: 563-572.
5) Kawabata I, Imai H, Kanno Z, Tetsumura A, Tsutsumi Y, Doi H, *et al*. Three-dimensional quantification of magnetic resonance imaging artifacts associated with shape factors. Dent Mater J 2019; 38: 638-645.
6) Imai H, Tanaka Y, Nomura N, Doi H, Tsutsumi Y, Ono T, *et al*. Magnetic susceptibility, artifact volume in MRI, and tensile properties of swaged Zr-Ag composites for biomedical applications. J Mech Behav Biomed Mater 2017; 66: 152-158.
7) Kondo R, Nomura N, Tsutsumi Y, Doi H, Hanawa T. Microstructure and mechanical properties of as-cast Zr-Nb alloys. Acta Biomater 2011; 7: 4278-4284.
8) Nomura N, Tanaka Y, Kondo R, Doi H, Tsutsumi Y, Hanawa T. Effects of phase constitution of Zr-Nb alloys on their magnetic susceptibilities. Mater Trans 2009; 50: 2466-2472.
9) Nomura N, Oya K, Tanaka Y, Kondo R, Doi H, Tsutsumi Y, *et al*. Microstructure and magnetic susceptibility of as-cast Zr-Mo alloys, Acta Biomater 2010; 6: 1033-1038.
10) Ashida M, Sugimoto T, Nomura N, Tsutsumi Y, Chen P, Doi

H, *et al*. Microstructure and mechanical properties of large-scale ingots of the Zr-1Mo alloy. Mater Trans 2015; 56: 1544-1548.
11) Tsutsumi Y, Nishisaka T, Doi H, Ashida M, Chen P, Hanawa T. Reaction of calcium and phosphate ions with titanium, zirconium, niobium, and tantalum. Surf Interface Anal 2015; 47: 1148-1154.
12) Ashida M, Tsutsumi Y, Homma K, Chen P, Shimojo M, Hanawa T. Design of zirconium quaternary system alloys and their properties. Mater Trans 2020; 61: 776-781.
13) Hanawa T. Metals and medicine. Mater Trans 2021; 62: 139-148.
14) Sato H, Chen P, Ashida M, Tsutsumi Y, Harada H, Hanawa T. Evaluation of cytocompatibility and osteoconductivity of Zr-14Nb-5Ta-1Mo alloy with MC3T3-E1 cells. Dent Mater J 2022; 41: 421-428.
15) Manaka T, Tsutsumi Y, Ashida M, Chen P, Katayama H, Hanawa T. Development of electrochemical surface treatment for improvement of localized corrosion resistance of zirconium in chloride environment. Mater Trans 2021; 62: 788-796.
16) Manaka T, Tsutsumi Y, Takada Y, Chen P, Ashida M, Doi K, *et al*. Galvanic corrosion among Ti-6Al-4V ELI Alloy, Co-Cr-Mo Alloy, 316L-Type stainless steel, and Zr-1Mo Alloy for orthopedic implants. Mater Trans 2023; 64: 131-137.
17) Manaka T, Tsutsumi Y, Chen P, Ashida M, Katayama H, Hanawa T. Development of electrochemical surface treatment to visualize critical corrosion-inducing inclusions of Zr in chloride environments. J Electrochem Soc 2021; 168: 121505.
18) Tsutsumi Y, Muto I, Nakano S, Tsukada J, Manaka T, Chen P, *et al*. Effect of impurity elements on localized corrosion of zirconium in chloride containing environment. J Electrochem Soc 2020; 167: 141507.
19) Tanaka Y, Kobayashi E, Hiromoto S, Asami K, Imai H, Hanawa T. Calcium phosphate formation on titanium by low-voltage electrolytic treatments. J Mater Sci Mater Med 2007; 18: 797-806.
20) Végh J. The Shirley background revised. J Electron Spectrosc Relat Phenom 2006; 151: 159-164.
21) Asami K, Hashimoto K. An XPS study of the surfaces on Fe-Cr, Fe-Co and Fe-Ni alloys after mechanical polishing. Corrosion Sci 1984; 24: 83-97.
22) Asami K, Hashimoto K, Shimodaira S. XPS determination of compositions of alloy surfaces and surface oxides on mechanically polished iron-chromium alloys. Corrosion Sci 1977; 17: 713-723.
23) Scofield JH. Hartree-Slater subshell photoionization cross-sections at 1254 and 1487 eV. J Electron Spectrosc Relat Phenom 1976; 8: 129-137.
24) Reddy BM, Sreekanth PM, Yamada Y, Xu X, Kobayashi T. Surface characterization of sulfate, molybdate, and tungstate promoted $TiO_2$-$ZrO_2$ solid acid catalysts by XPS and other techniques. Appl Catal A 2002; 228: 269-278.
25) Reddy BM, Chowdhury B, Reddy EP, Fernández A. Characterization of $MoO_3$/$TiO_2$-$ZrO_2$ catalysts by XPS and other techniques. J Mol Catal A Chem 2000; 162: 431-441.
26) Petrik P, Sulyok A, Novotny T, Perez-Feró E, Kalas B, Agocs E, *et al*. Optical properties of Zr and $ZrO_2$. Appl Surf Sci 2017; 421: 744-747.
27) Song Z, Bao X, Wild U, Muhler M, Ertl G. Oxidation of amorphous Ni-Zr alloys studied by XPS, UPS, ISS and XRD. Appl Surf Sci 1998; 134: 31-38.
28) Reddy BM, Chowdhury B, Ganesh I, Reddy EP, Rojas TC, Fernández A. Characterization of $V_2O_5$/$TiO_2$-$ZrO_2$ catalysts by XPS and other techniques. J Phys Chem B 1998; 102: 10176-10182.
29) Ge XQ, Wang YG, Shao JQ, Wei W, Zhang B, Wang SH, *et al*. Testing the activation temperature of non-evaporable Ti-Zr-Hf-V getter films by XPS. Nucl Instr Meth Phys Res A 2020; 967: 163864.
30) Zhang WB, Wu WD, Wang XM, Cheng XL, Yan DW, Shen CL, *et al*. The investigation of $NbO_2$ and $Nb_2O_5$ electronic structure by XPS, UPS and first principles methods. Surf Interface Anal 2013; 45: 1206-1210.
31) Milosev I, Kosec T, Strehblow HH. XPS and EIS study of the passive film formed on orthopaedic Ti-6Al-7Nb alloy in Hank's physiological solution. Electrochim Acta 2008; 53: 3547-3558.
32) Hryniewicz T, Rokosz K, Sandim HRZ. SEM/EDX and XPS studies of niobium after electropolishing. Appl Surf Sci 2012; 263: 357-361.
33) Alov NV. Surface oxidation of metals by oxygen ion bombardment, Nucl Instr Meth Phys Res B 2007; 256: 337-340.
34) Lu Y, Le Breton JC, Turban P, Lépine B, Schieffer P, Jézéquel G. Band structure of the epitaxial Fe/MgO/GaAs(001) tunnel junction studied by X-ray and ultraviolet photoelectron spectroscopies. Appl Phys Lett 2006; 89: 152106.
35) Veal BW, Lam DJ, Westlake DG. X-ray photoemission spectroscopy study of zirconium hydride. Phys Rev B 1979; 19: 2856-2863.
36) Magnuson M, Schmidt S, Hultman L, Högberg H. Electronic properties and bonding in $ZrH_x$ thin films investigated by valence-band X-ray photoelectron spectroscopy. Phys Rev B 2017; 96: 195103.
37) Khanuja M, Sharma H, Mehta BR, Shivaprasad SM. XPS depth-profile of the suboxide distribution at the native oxide/Ta interface. J Electron Spectrosc Relat Phenom 2009; 169: 41-45.
38) Kerrec O, Devilliers D, Groult H, Marcus P. Study of dry and electrogenerated $Ta_2O_5$ and Ta/$Ta_2O_5$/Pt structures by XPS. Mater Sci Eng B 1998; 55: 134-142.
39) Zier M, Oswald S, Reiche R, Kozlowska M, Wetzig K. Interface formation and reactions at Ta-Si and Ta-$SiO_2$ interfaces studied by XPS and ARXPS. J Electron Spectrosc Relat Phenom 2004; 137: 229-233.
40) Medicherla VRR, Majumder S, Paramanik D, Varma S. Formation of self-organized Ta nano-structures by argon ion sputtering of Ta foil: XPS and AFM study. J Electron Spectrosc Relat Phenom 2010; 180: 1-5.
41) Moo JGS, Awaludin Z, Okajima T, Ohsaka T. An XPS depth-profile study on electrochemically deposited $TaO_x$. J Solid State Electrochem 2013; 17: 3115-3123.
42) Samuel S, Nag S, Nasrazadani S, Ukirde V, El Bouanani M, Mohandas A, *et al*. Corrosion resistance and *in vitro* response of laser-deposited Ti-Nb-Zr-Ta alloys for orthopedic implant applications. J Biomed Mater Res A 2010; 94A: 1251-1256.
43) Brunckova H, Kanuchova M, Kolev H, Mudra E, Medvecky L. XPS characterization of $SmNbO_4$ and $SmTaO_4$ precursors prepared by sol-gel method. Appl Surf Sci 2019; 473: 1-5.
44) Rokosz K, Hryniewicz T, Chapon P, Raaen S, Sandim HRZ. XPS and GDOES characterization of porous coating enriched with copper and calcium obtained on tantalum via plasma electrolytic oxidation. J Spectrosc 2016; 2016: 7093071.
45) Choi JG, Thompson LT. XPS study of as-prepared and reduced molybdenum oxides. Appl Surf Sci 1996; 93: 143-149.
46) Delporte P, Meunier F, Phamhuu C, Vennegues P, Ledoux MJ, Guille J. Physical characterization of molybdenum oxycarbide catalyst; TEM, XRD and XPS. Catal Today 1995; 23: 251-267.
47) Hanawa T, Hiromoto S, Asami K. Characterization of the surface oxide film of a Co-Cr-Mo alloy after being located in quasi-biological environments using XPS. Appl Surf Sci 2001; 183: 68-75.
48) Tsutsumi Y, Bártáková S, Prachár P, Migita S, Doi H, Nomura N, *et al*. Long-term corrosion behavior of biocompatible beta-type Ti alloy in simulated body fluid. J Electrochem Soc 2012; 159: C435-C440.